


 Cite this: *RSC Adv.*, 2023, **13**, 21754

Synthesis of $\text{AgBr}/\text{Ti}_3\text{C}_2@\text{TiO}_2$ ternary composite for photocatalytic dehydrogenation of 1,4-dihydropyridine and photocatalytic degradation of tetracycline hydrochloride

 Hanliu Wu,^a Yan Quan,^a Meiling Liu,^a Xuemei Tian,^a Chunguang Ren^b and Zhonghua Wang  ^{id} ^{*a}

In this work, $\text{AgBr}/\text{Ti}_3\text{C}_2@\text{TiO}_2$ ternary composite photocatalyst was prepared by a solvothermal and precipitation method with the aims of introducing Ti_3C_2 as a cocatalyst and TiO_2 as a compositing semiconductor. The crystal structure, morphology, elemental state, functional groups and photoelectrochemical properties were studied by XRD, SEM, TEM, XPS, FI-IR and EIS. The photocatalytic performances of the composites were investigated by the photodehydrogenation of diethyl 1,4-dihydro-2,6-dimethyl-3,5-pyridinedicarboxylate (1,4-DHP) and the photodegradation of tetracycline hydrochloride (TCH) under visible light irradiation ($\lambda > 400$ nm). The $\text{AgBr}/\text{Ti}_3\text{C}_2@\text{TiO}_2$ composite photocatalyst showed enhanced photocatalytic performance in both photocatalytic reactions. The photocatalytic activity of the composite photocatalyst is dependent on the proportional content of $\text{Ti}_3\text{C}_2@\text{TiO}_2$. With optimized $\text{Ti}_3\text{C}_2@\text{TiO}_2$ proportion, the photocatalytic ability of the $\text{AgBr}/\text{Ti}_3\text{C}_2@\text{TiO}_2$ composite was 24.5 times as high as that of $\text{Ti}_3\text{C}_2@\text{TiO}_2$ for photodehydrogenation of 1,4-DHP and 1.9 times as high as that of pure AgBr for photodegradation of TCH. The enhanced photocatalytic performance of the $\text{AgBr}/\text{Ti}_3\text{C}_2@\text{TiO}_2$ composite should be due to the formation of a p-n heterojunction structure between AgBr and $\text{Ti}_3\text{C}_2@\text{TiO}_2$ and the excellent electronic properties of Ti_3C_2 , which enhanced the visible light absorption capacity, lowered the internal resistance, speeded up the charge transfer and reduced the recombination efficiency of photo-generated carriers. Mechanism studies showed that superoxide free radical (O_2^-) was the main active species. In addition, the composite photocatalyst also displayed good stability, indicating its reutilization in practical application.

Received 2nd April 2023

Accepted 10th July 2023

DOI: 10.1039/d3ra02164e

rsc.li/rsc-advances

1. Introduction

With the rapid development of industrialization and urbanization, environmental pollution and the energy crisis have received extensive attention in the past decades.¹⁻³ In order to solve these problems, inexhaustible solar-driven photocatalysis is considered to be a potential green method to produce photoinduced carriers with redox ability by using semiconductors as photocatalysts.^{4,5} So far, many photocatalysts have been reported in this field, such as TiO_2 ,^{6,7} ZnO ,⁸ CdS ^{9,10} and $\text{g-C}_3\text{N}_4$.^{11,12} Among these photocatalysts, TiO_2 has gained a lot of attention due to its high photocatalytic ability and good chemical stability. What's more, it is also low in price and easy to obtain, safe and harmless.¹³ However, the practical application of TiO_2 as a photocatalyst is limited because it can only be

excited by UV light that accounts for only a small fraction of the natural sunlight (~5%).^{14,15} The method to overcome this shortcoming is to modify TiO_2 with narrow band gap semiconductors. Under light irradiation, the photogenerated charge carriers can move from one semiconductor to another, thereby enhancing the photocatalytic activity.¹⁶⁻¹⁸

AgBr is an important photosensitive semiconductor for traditional use. It is an n-type semiconductor with a narrow band gap of ~2.64 eV and is very active under visible light excitation.¹⁷ Unfortunately, the pure AgBr is quite unstable, and the photoinduced electrons will combine with Ag^+ to form Ag^0 clusters, resulting in the undesirable and uncontrolled photolysis of AgBr , which leads to the low reusability of AgBr in photocatalytic reaction.¹⁹⁻²¹ Therefore, the composite of AgBr and TiO_2 can enhance the photocatalytic performance and improve the photocatalytic stability by reducing the band gap and prolonging the life of photoinduced electron-hole pairs. Abou Asi *et al.* prepared AgBr/TiO_2 nanocomposite by a deposition-precipitation method with the addition of cetyltrimethylammonium bromide, and evaluated the photocatalytic

^aChemical Synthesis and Pollution Control Key Laboratory of Sichuan Province, College of Chemistry and Chemical Engineering, China West Normal University, Nanchong 637002, Sichuan, China. E-mail: zhwangs@163.com; Fax: +86 817-2568081; Tel: +86 817-2445233

^bCollege of Life Sciences, Yantai University, Yantai 264005, China



activity by the reduction of CO_2 .²² Cui *et al.* successfully prepared AgBr nanoparticles modified TiO_2 nanotube arrays (AgBr/ TiO_2 NTAs) photoelectrode by anodic oxidation and ultrasonic assisted precipitation. The enhance photocatalytic activity of the AgBr/ TiO_2 NTAs materials was evaluated by the degradation of 4-chlorophenol (4-CP) under visible light irradiation, and 92.6% of 4-CP degradation was obtained within 140 min of Xenon illumination.²³

MXene, a new family of 2D transition metal carbides and/or nitrides, has attracted widespread interest since its first appearance in 2011.²⁴ Up to now, MXenes has been widely studied and applied in energy storage and conversion,²⁵ catalysis,²⁶ sensor,²⁷ heavy metal ion²⁸ and dye adsorption²⁹ and other fields. Because of the excellent conductivity and well visible light absorption capacity of Ti_3C_2 MXene, it has been clearly proved to be an efficient cocatalyst for improving photocatalytic activity, which can effectively promote the separation and transfer of photogenerated electrons. For example, Low *et al.* used the calcination method to grow TiO_2 nanoparticles *in situ* on Ti_3C_2 MXene with good electrical conductivity. The photocatalytic reduction of CO_2 to CH_4 ($0.22 \mu\text{mol h}^{-1}$) by the optimized $\text{TiO}_2/\text{Ti}_3\text{C}_2$ composite is 3.7 times higher than that of commercial TiO_2 (P25).³⁰ Moreover, Li *et al.* modified carbon nitride (CN) with Ti_3C_2 and found that compared with the original CN, the modified CN showed significantly improved photocatalytic activity for U(vi) reduction.²

To the best of our knowledge, there is no report about the enhancement of the photocatalytic performance of AgBr by compositing with TiO_2 and simultaneously introducing Ti_3C_2 as a cocatalyst. In this study, $\text{Ti}_3\text{C}_2@\text{TiO}_2$ was prepared by *in situ* growth of TiO_2 on Ti_3C_2 under solvothermal treatment, and a series of AgBr/ $\text{Ti}_3\text{C}_2@\text{TiO}_2$ composites were prepared by precipitation method. The *in situ* preparation of $\text{Ti}_3\text{C}_2@\text{TiO}_2$ makes Ti_3C_2 and TiO_2 closely contact, and improves the separation efficiency of photogenerated electron hole pairs. The photocatalytic performance of the AgBr/ $\text{Ti}_3\text{C}_2@\text{TiO}_2$ photocatalyst was evaluated by the photodehydrogenation of 1,4-DHP and photodegradation of TCH under visible light irradiation. The AgBr/ $\text{Ti}_3\text{C}_2@\text{TiO}_2$ photocatalyst showed enhanced photocatalytic performance in both photocatalytic reactions. The photocatalytic performance of the AgBr/ $\text{Ti}_3\text{C}_2@\text{TiO}_2$ composite with optimized composition is 3.9 and 24.5 times higher than that of pure AgBr and $\text{Ti}_3\text{C}_2@\text{TiO}_2$, respectively, for photodehydrogenation of 1,4-DHP and 1.9 and 5.9 times higher than that of pure AgBr and $\text{Ti}_3\text{C}_2@\text{TiO}_2$ for photodegradation of TCH. The composite photocatalyst were stable under light irradiation. The relative dehydrogenation efficiency of 1,4-DHP photolysis and the relative degradation efficiency of TCH degradation remained above 86% after four cycles.

2. Experimental

2.1. Preparation of AgBr powder

First, 1.0 g AgNO_3 was dissolved in 50 mL of deionized water to obtain AgNO_3 solution (solution A), 0.70 g KBr was mixed with 25 mL deionized water and dissolved to prepare KBr solution (solution B). Then, the solution B was added dropwise the

solution A under magnetically stirring, and the mixed solution was stirred in the dark for 0.5 h. After centrifugation and washing, the AgBr precipitate was collected and dried at 60 °C.

2.2. Preparation of layered Ti_3C_2

Typically, 0.5 g Ti_3AlC_2 powder was added to 10 mL 30 wt% HF (within 5 min) and the reaction was allowed to proceed at room temperature for 5 h to remove the element of Al. The resulting powder was collected by centrifugation (3500 rpm, 5 min per cycle) and washed 5 times with deionized water. Then, the black precipitate was dried at 80 °C for 24 h to obtain multilayered Ti_3C_2 .

2.3. Preparation of $\text{Ti}_3\text{C}_2@\text{TiO}_2$ by *in situ* solvothermal method

First, 0.3 g Ti_3C_2 , which was obtained from HF etching of Ti_3AlC_2 , was mixed with 30 mL isopropanol (IPA). After sonication for 10 min, the mixture was poured into a 100 mL Teflon-lined reactor and heated at 150 °C for 24 h. The precipitate was centrifuged, repeatedly washed until the pH value of the eluate was about 6, and then dried at 60 °C to obtain $\text{Ti}_3\text{C}_2@\text{TiO}_2$ sample.

2.4. Preparation of AgBr/ $\text{Ti}_3\text{C}_2@\text{TiO}_2$ composites

Solution A was prepared by dissolving 0.1808 g AgNO_3 and dispersing 0.0225 g $\text{Ti}_3\text{C}_2@\text{TiO}_2$ to 50 mL deionized water. Solution B was prepared by dissolving 0.1267 g KBr to 25 mL of deionized water. Then, solution B was added dropwise to solution A under magnetic stirring. After further stirred for 2 h, the reaction mixture was centrifuged, filtered and dried at 60 °C to obtain AgBr/ $\text{Ti}_3\text{C}_2@\text{TiO}_2$ composite. This sample was denoted as AgBr/ $\text{Ti}_3\text{C}_2@\text{TiO}_2$ -10%, for the mass percentage of $\text{Ti}_3\text{C}_2@\text{TiO}_2$ was accounting for 10% of the sample. Other AgBr/ $\text{Ti}_3\text{C}_2@\text{TiO}_2$ composite samples with different proportions of $\text{Ti}_3\text{C}_2@\text{TiO}_2$ (10%, 20%, 30%, 40%, 50%, 60%, 70%) were prepared by changing the amount of each sample. The obtained AgBr/ $\text{Ti}_3\text{C}_2@\text{TiO}_2$ samples were denoted as AgBr/ $\text{Ti}_3\text{C}_2@\text{TiO}_2$ -x% (x% referred to the mass percentage of $\text{Ti}_3\text{C}_2@\text{TiO}_2$).

2.5. Characterization

The crystal structure, morphology, and elemental composition were characterized by X-ray diffraction (XRD), scanning electron microscopy (SEM), high-resolution transmission electron microscopy (HRTEM), energy dispersive spectrometer (EDS), X-ray photoelectron spectroscopy (XPS) and Fourier transform infrared spectrometer (FT-IR). An electrochemical workstation equipped with a three-electrode system was used to measure the electrochemical characteristics of the samples.

2.6. Photocatalytic performance evaluation

The photocatalytic performance of AgBr/ $\text{Ti}_3\text{C}_2@\text{TiO}_2$ was evaluated by the photodehydrogenation of 1,4-DHP and photodegradation of TCH under the irradiation of visible light. The light was provided by a 70 W metal halide lamp equipped with a 400 nm cutoff filter. Typically, 50 mg of AgBr/ $\text{Ti}_3\text{C}_2@\text{TiO}_2$



composite was dispersed into 50 mL of 0.1 mM 1,4-DHP or 20 mg L⁻¹ TCH solution. In order to obtain adsorption-desorption equilibrium, the mixture was magnetically stirred for 30 min before illumination. The extent of the reaction was spectroscopically monitored by measuring the residual concentrations of 1,4-DHP and TCH at wavelengths of 374 and 357 nm, respectively.

3. Results and discussion

The XRD patterns of Ti_3AlC_2 , Ti_3C_2 , $\text{Ti}_3\text{C}_2@\text{TiO}_2$, AgBr and AgBr/ $\text{Ti}_3\text{C}_2@\text{TiO}_2$ composites are shown in Fig. 1. Ti_3C_2 was obtained by etching Ti_3AlC_2 with HF, removing Al layer and retaining Ti and C layers, the XRD diffraction pattern of the precursor Ti_3AlC_2 shows that there was a main diffraction peak at $2\theta = 39.3^\circ$. After reacting with HF, the diffraction pattern had undergone the following significant changes: firstly, the peak observed at the diffraction angle of $2\theta = 39.3^\circ$ almost disappeared, indicating that the Al layer was successfully removed by etching.³¹ Secondly, at the low diffraction angle, because of the expansion of the interlayer distance, the peaks at (002) and (004) move to a low angle and become wider and weaker, indicating that Ti_3AlC_2 has been transformed into Ti_3C_2 .^{32,33} The characteristic peaks of multilayer Ti_3C_2 appear at 2θ values of 8.94° (002), 18.29° (006), 27.66° (008), 34.53° (101), 41.78° (105) and 60.62° (110), which are consistent with the literature.^{34,35} $\text{Ti}_3\text{C}_2@\text{TiO}_2$ composites were obtained by *in situ* growth of TiO_2 on Ti_3C_2 after solvothermal treatment of Ti_3C_2 and isopropanol (IPA) in a reactor. The characteristic peaks at 25.28° , 36.95° , 48.04° and 55.06° were attributed to the (101), (103), (200) and (211) crystal planes of anatase TiO_2 (JCPDS no. 21-1272).³⁶ And the characteristic peaks with 2θ values of 8.94° , 18.29° , 27.66° , 34.53° and 60.62° in $\text{Ti}_3\text{C}_2@\text{TiO}_2$ correspond to the (002), (004), (006), (101) and (110) crystal planes of Ti_3C_2 , respectively. These results indicate that $\text{Ti}_3\text{C}_2@\text{TiO}_2$ composites were successfully synthesized (Fig. 1A). It can be noted from Fig. 1B that the diffraction peaks of AgBr can be attributed to the face-centered cubic crystal phase of AgBr, and the 2θ values are 26.72° (111), 30.96° (200), 44.34° (220), 52.48° (311), 55.04° (222), 64.47°

(400), 71.09° (331), 73.26° (420) and 81.61° (422), respectively.¹⁷ It is consistent with the standard data of AgBr (JCPDS no. 06-0438). As for the AgBr/ $\text{Ti}_3\text{C}_2@\text{TiO}_2$ composites, except for the XRD patterns of AgBr, another two peaks appeared at 2θ values of 39.12° and 77.39° , which should be ascribed to the (111) and (311) crystal planes of Ag^0 (JCPDS no. 65-2871)^{33,37} (Fig. 1B). With the increase of $\text{Ti}_3\text{C}_2@\text{TiO}_2$ content, the diffraction peaks of AgBr in the ternary composites gradually weakened, and the diffraction peaks of (111) and (311) crystal planes of Ag increased. Due to the existence of low-valent Ti with strong reducing activity in Ti_3C_2 solution, Ag^+ can be partially reduced to Ag^0 .^{33,38} It is worth noting that the XRD peaks of Ti_3C_2 and TiO_2 were not observed in the XRD patterns of AgBr/ $\text{Ti}_3\text{C}_2@\text{TiO}_2$ composites, which may have resulted from their low degree of crystallization in the composite samples.^{39,40}

As shown in Fig. 2A and B, due to the exothermic reaction of HF, Ti_3AlC_2 transforms from a dense, layered ternary carbide structure to an accordion-like structure of Ti_3C_2 .³⁵ After co-heat treatment of Ti_3C_2 and isopropanol (IPA) in a reactor, TiO_2 nanosheets with a size of about 100 nm were *in situ* grown on the surface of multilayer Ti_3C_2 to form $\text{Ti}_3\text{C}_2@\text{TiO}_2$ composites (Fig. 2C). The AgBr sample shows that irregular polyhedrons with a size of about 2–4 μm were clustered together (Fig. 2D). Compared with pure AgBr (Fig. 2D), AgBr particles in AgBr/ $\text{Ti}_3\text{C}_2@\text{TiO}_2$ -10% samples showed better dispersibility and smaller size (Fig. 2E). With the increase of $\text{Ti}_3\text{C}_2@\text{TiO}_2$ content, the shape of irregular polyhedral AgBr particles becomes more dispersed and the particle size becomes smaller (Fig. 2F). These results indicate that the addition of $\text{Ti}_3\text{C}_2@\text{TiO}_2$ not only affects the morphology and size of AgBr particles, but also prevents the agglomeration of AgBr polyhedral.

The microstructure of AgBr/ $\text{Ti}_3\text{C}_2@\text{TiO}_2$ -40% composite was further analyzed by TEM and HRTEM. As shown in Fig. 3A and B, AgBr is in close contact with the $\text{Ti}_3\text{C}_2@\text{TiO}_2$ sheets. According to Fig. 3C, the lattice fringe spacing of 0.189 nm and 0.204 nm correspond to the TiO_2 (200) and AgBr (200) crystal planes, respectively. The lattice fringe spacings of 0.189 nm and 0.230 nm belong to TiO_2 (200) and Ti_3C_2 (103) crystal planes, respectively³¹ (Fig. 3E). Furthermore, the lattice fringes at

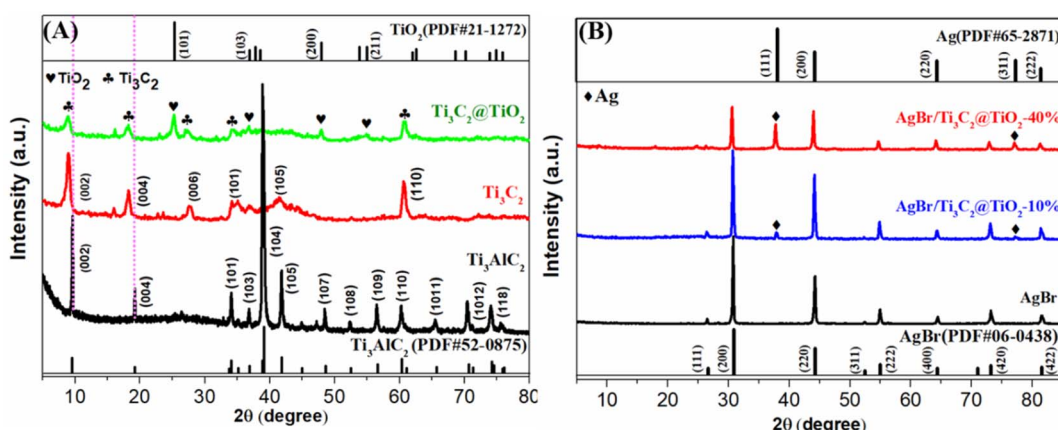


Fig. 1 XRD patterns of Ti_3AlC_2 , Ti_3C_2 and $\text{Ti}_3\text{C}_2@\text{TiO}_2$ (A), AgBr and AgBr/ $\text{Ti}_3\text{C}_2@\text{TiO}_2$ composites (B).



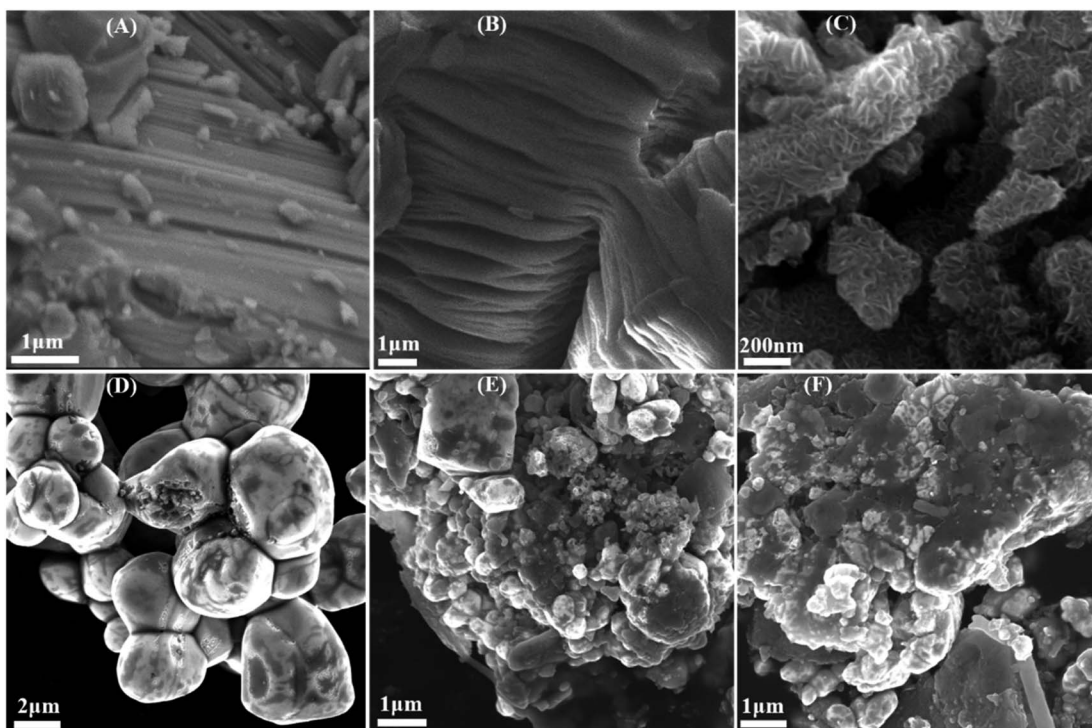


Fig. 2 SEM images of Ti_3AlC_2 (A), Ti_3C_2 (B), $\text{Ti}_3\text{C}_2@\text{TiO}_2$ (C), AgBr (D), $\text{AgBr}/\text{Ti}_3\text{C}_2@\text{TiO}_2\text{-}10\%$ (E), $\text{AgBr}/\text{Ti}_3\text{C}_2@\text{TiO}_2\text{-}40\%$ (F).

0.214 nm and 0.204 nm correspond to Ti_3C_2 (005) and Ag (200) crystal planes, respectively⁴¹ (Fig. 3D and F). The above data show that after solvothermal method and precipitation method, stable heterojunctions are formed between AgBr and TiO_2 , thus improving the photocatalytic performance of the composites.⁴²

The element distribution and composition of the composites were detected by elemental mapping image. Fig. 4 shows the

elemental scanning spectrum of $\text{AgBr}/\text{Ti}_3\text{C}_2@\text{TiO}_2\text{-}10\%$ composites. As can be seen from the figure, the distribution of six elements, namely C, Ag, Br, O, Ti and F. Among them, the element F is the residue of Ti_3AlC_2 etched by HF, so its content is less.

The full XPS spectra (Fig. 5A) shows the characteristic peaks of Ti, C, O, Ag and Br in $\text{AgBr}/\text{Ti}_3\text{C}_2@\text{TiO}_2\text{-}40\%$ sample. Fig. 5B–

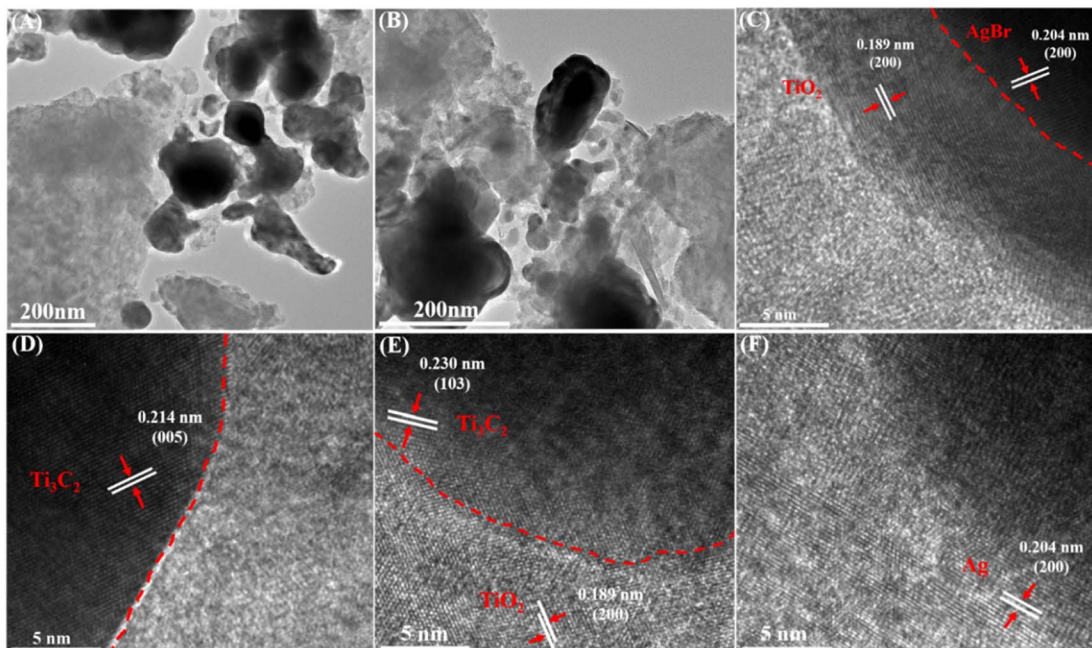


Fig. 3 TEM (A and B) and HRTEM (C, D, E and F) images of $\text{AgBr}/\text{Ti}_3\text{C}_2@\text{TiO}_2\text{-}40\%$ sample.

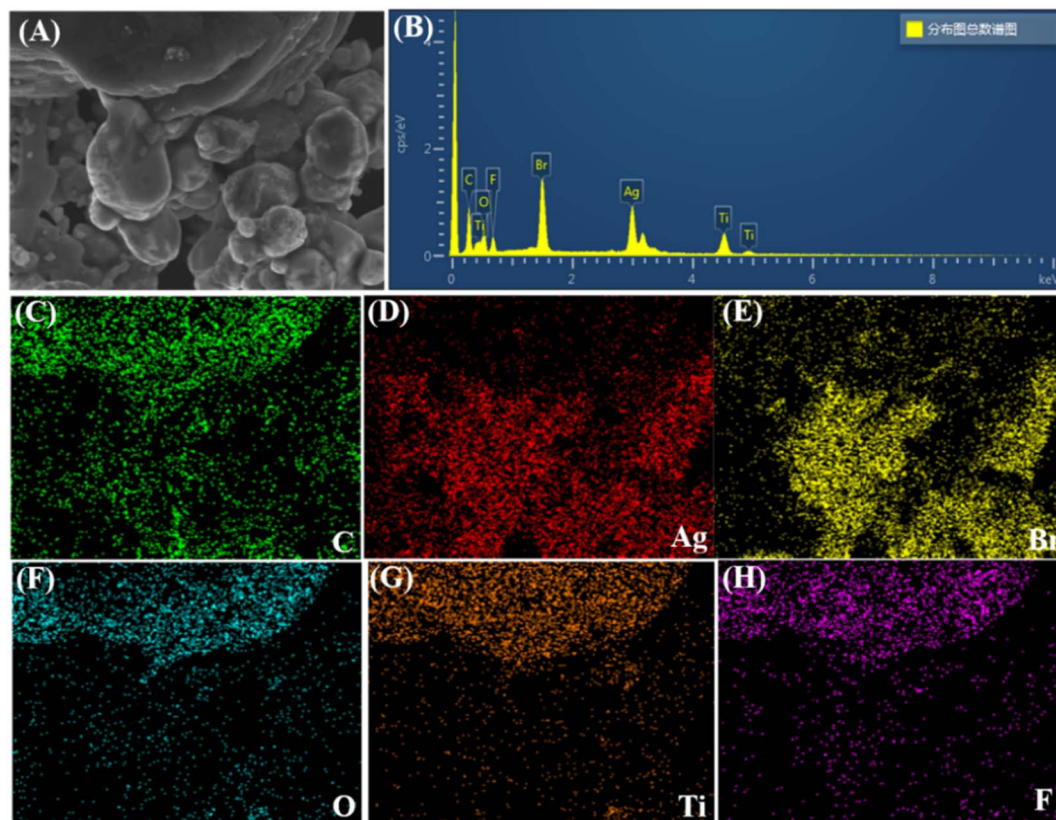


Fig. 4 Selected SEM images (A), the EDS spectrum of the AgBr/Ti₃C₂@TiO₂-10% composite (B), C (C), Ag (D), Br (E), O (F), Ti (G) and F (H) element.

F shows the high-resolution spectra of each element. After carbon correction, curve fitting and background subtraction are carried out. As shown in Fig. 5B, five different peaks can be found in high resolution Ti 2p, of which 455.1 eV, 456.5 eV and 459.0 eV belong to Ti 2p_{3/2}, 464.8 eV and 461.6 eV attribute to Ti

2p_{1/2}. Specifically, the peaks at 456.5 eV, 459.0 eV and 464.8 eV can be belonged to Ti–O bond, and the peaks at 455.1 eV and 461.6 eV indicate the existence of Ti–C bond.^{43,44} The XPS C 1s spectrum of the composite (Fig. 5C) showed a strong peak at the binding energy of 284.8 eV, corresponding to the C–C bond.

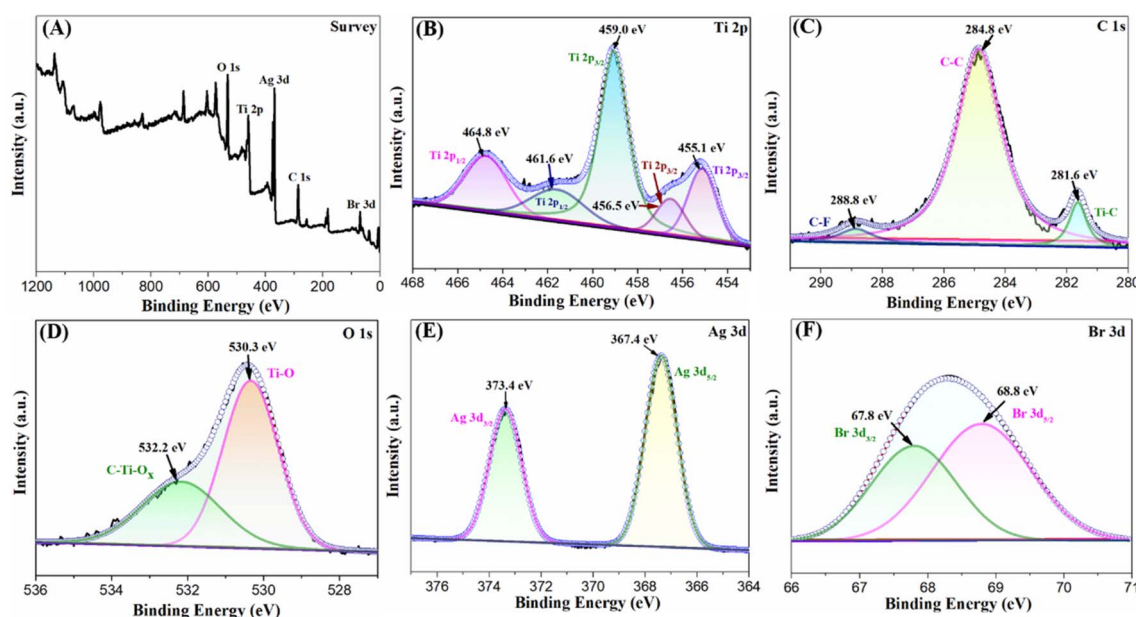


Fig. 5 High-resolution XPS spectra of the AgBr/Ti₃C₂@TiO₂-40%. Full spectrum (A), Ti 2p (B), C 1s (C), O 1s (D), Ag 3d (E) and (F) Br 3d.

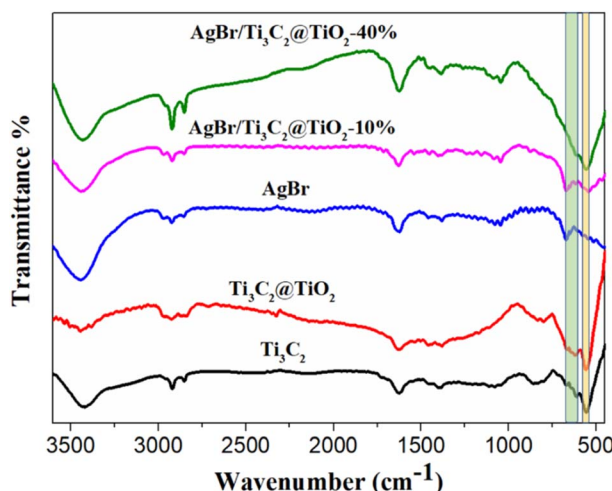


Fig. 6 FT-IR spectra of Ti_3C_2 , $\text{Ti}_3\text{C}_2@\text{TiO}_2$, AgBr , $\text{AgBr}/\text{Ti}_3\text{C}_2@\text{TiO}_2$ -10% and $\text{AgBr}/\text{Ti}_3\text{C}_2@\text{TiO}_2$ -40% samples.

Two peaks appear at the binding energies of 281.6 eV and 288.8 eV, corresponding to the Ti-C bond and the C-F bond, respectively.^{43,45} In addition, the O 1s XPS spectrum showed two distinct peaks at 532.2 eV and 530.3 eV (Fig. 5D), the highest peak at 530.3 eV usually represent the lattice oxygen in TiO_2 , which also indicated that TiO_2 was successfully grown *in situ* on Ti_3C_2 .³¹ Fig. 5E shows the Ag 3d spectrum. There are two peaks

at around 367.4 eV and 373.4 eV, which can be attributed to $\text{Ag 3d}_{5/2}$ and $\text{Ag 3d}_{3/2}$, respectively. Other studies have shown that the $\text{Ag 3d}_{5/2}$ and $\text{Ag 3d}_{3/2}$ peaks of Ag^+ in AgBr usually locate at about 367.37 and 373.48 eV, and the $\text{Ag 3d}_{5/2}$ and $\text{Ag 3d}_{3/2}$ peaks of Ag^0 are usually observed at 367.87 and 376.03 eV.¹⁴ The present Ag 3d data (367.4 eV for $\text{Ag 3d}_{5/2}$ and 373.4 eV for $\text{Ag 3d}_{3/2}$) should be the superposition of the 3d binding energy of Ag^0 and Ag^+ .⁴⁶ However, the peaks in Fig. 5E are difficult to divide into two sets of peaks belonging to Ag^0 and Ag^+ , respectively. It may show that Ag^0 particles and AgBr particles have a special composite structure, which is different from any of their individual particles.^{37,46} Fig. 5F shows the Br 3d XPS spectrum, the binding energies of 67.8 eV and 68.8 eV correspond to $\text{Br 3d}_{3/2}$ and $\text{Br 3d}_{5/2}$, respectively.^{47,48}

The functional groups of Ti_3C_2 , $\text{Ti}_3\text{C}_2@\text{TiO}_2$, AgBr , $\text{AgBr}/\text{Ti}_3\text{C}_2@\text{TiO}_2$ -10% and $\text{AgBr}/\text{Ti}_3\text{C}_2@\text{TiO}_2$ -40% were detected by FT-IR (Fig. 6). The absorption peaks appeared at 3424 cm^{-1} and 1631 cm^{-1} , respectively, corresponding to $-\text{OH}$ asymmetric stretching and $-\text{OH}$ bending vibration of adsorbed water.⁴⁹ Furthermore, the band at about 2850 cm^{-1} – 2924 cm^{-1} corresponds to O-H stretching vibration, which reflects the existence of $-\text{OH}$.⁵⁰ In $\text{Ti}_3\text{C}_2@\text{TiO}_2$, the peaks at 616 cm^{-1} and 564 cm^{-1} correspond to Ti-O and Ti-C vibrations respectively,^{26,51} and the peak at 1393 cm^{-1} corresponds to C-O or C-N.⁵² With the increase of $\text{Ti}_3\text{C}_2@\text{TiO}_2$ content, the two characteristic peaks of Ti_3C_2 (at 564 cm^{-1} – 670 cm^{-1}) gradually increased when it was compounded with AgBr .

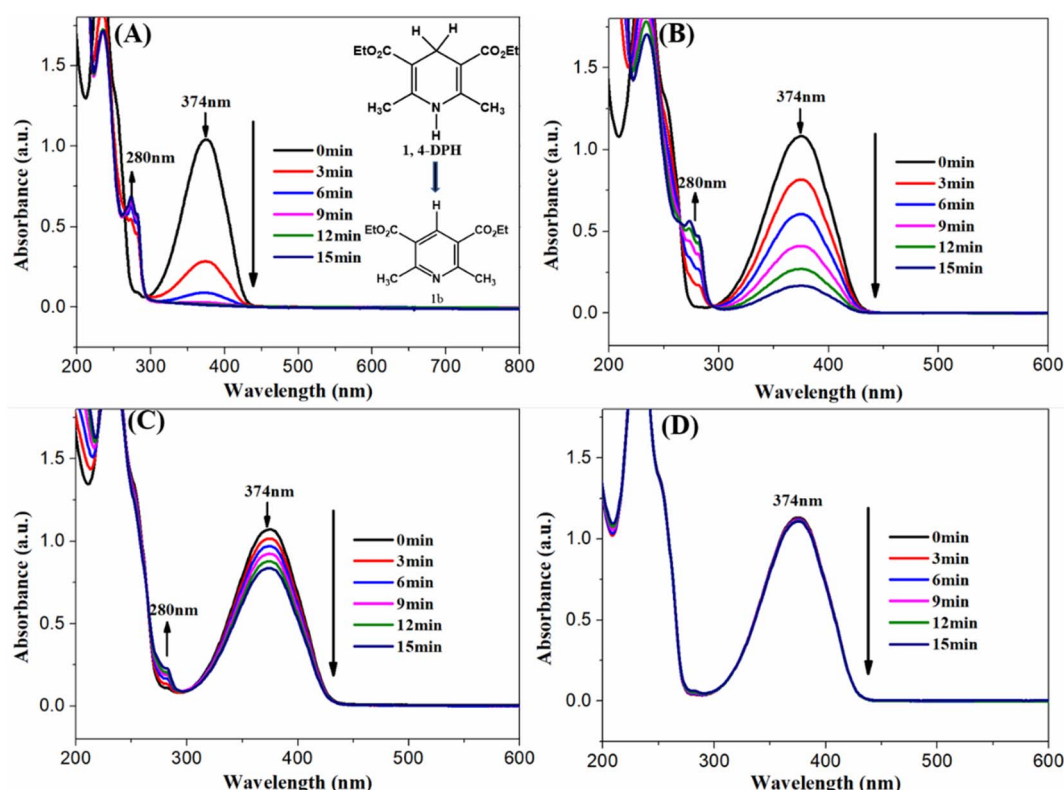


Fig. 7 Under the irradiation of visible light ($\lambda > 400\text{ nm}$), the ultraviolet-visible spectrum changes of 1,4-DHP solution under different photo-catalysts. (A) $\text{AgBr}/\text{Ti}_3\text{C}_2@\text{TiO}_2$ -40%, (B) AgBr , (C) $\text{Ti}_3\text{C}_2@\text{TiO}_2$ and (D) no catalyst.



The photocatalytic performance of the prepared $\text{AgBr}/\text{Ti}_3\text{C}_2@\text{TiO}_2$ composite was tested by the dehydrogenation of 1,4-DHP under visible light irradiation ($\lambda > 400$ nm). As shown in Fig. 7A, the absorption peak of 1,4-DHP at 374 nm decreased rapidly, accompanied with the rapid increase at 280 nm. According to the previous literature, the simultaneous peak intensity decrease at 374 nm and increase at 280 nm indicates the dehydrogenation of 1,4-DHP,^{53–55} namely the conversion of 1,4-DHP to its pyridine derivatives (Fig. 7A, inset). When AgBr and $\text{Ti}_3\text{C}_2@\text{TiO}_2$ were used as photocatalyst, the changes of the peak intensity at 374 and 280 nm were also observed, but the changes were much slower (Fig. 7B and C). When no catalyst was added and only irradiated under visible light, the changes of the two peaks were hardly observed. After 9 min irradiation under visible light, the conversion rate of 1,4-DHP were 98.9%, 84.5%, and 21.9% in the presence of $\text{AgBr}/\text{Ti}_3\text{C}_2@\text{TiO}_2$ -40%, AgBr , and $\text{Ti}_3\text{C}_2@\text{TiO}_2$ respectively. The above results show that the as-prepared $\text{AgBr}/\text{Ti}_3\text{C}_2@\text{TiO}_2$ composites have much better photocatalytic performance for 1,4-DHP photodehydrogenation.

In order to further analyze the influence of $\text{Ti}_3\text{C}_2@\text{TiO}_2$ content on the photocatalytic properties of $\text{AgBr}/\text{Ti}_3\text{C}_2@\text{TiO}_2$ composites, we prepared a series of $\text{AgBr}/\text{Ti}_3\text{C}_2@\text{TiO}_2$ composites with different $\text{Ti}_3\text{C}_2@\text{TiO}_2$ content and evaluated their photocatalytic activities by the photodehydrogenation of 1,4-DHP. With the increase of $\text{Ti}_3\text{C}_2@\text{TiO}_2$ content, the photocatalytic performance of the $\text{AgBr}/\text{Ti}_3\text{C}_2@\text{TiO}_2$ composites first increased and then decreased. All of the composites displayed enhanced photocatalytic ability and the $\text{AgBr}/\text{Ti}_3\text{C}_2@\text{TiO}_2$ -40% composite showed the highest photocatalytic activity (Fig. 8A and B). The rate constants of the photocatalyst for 1,4-DHP dehydrogenation are obtained by plotting $\ln(C/C_0)$ versus illumination time (Fig. 8C) and compared in Fig. 8D. The rate constant of $\text{AgBr}/\text{Ti}_3\text{C}_2@\text{TiO}_2$ -40% (0.4044 min^{-1}) is the highest, which is about 3.9 times and 24.5 times as high as that of pure AgBr (0.1035 min^{-1}) and $\text{Ti}_3\text{C}_2@\text{TiO}_2$ (0.0165 min^{-1}), respectively, further confirming the enhanced photocatalytic activity of $\text{AgBr}/\text{Ti}_3\text{C}_2@\text{TiO}_2$ composites.

Besides the photodehydrogenation of 1,4-DHP, the $\text{AgBr}/\text{Ti}_3\text{C}_2@\text{TiO}_2$ composites was further applied for the photodegradation of TCH under visible light irradiation ($\lambda > 400$ nm). As shown in Fig. 9A, when the catalyst is $\text{AgBr}/\text{Ti}_3\text{C}_2@\text{TiO}_2$ -10%, the absorption peak of TCH at 357 nm decreases rapidly, indicating the efficient catalytic degradation of TCH. When AgBr and $\text{Ti}_3\text{C}_2@\text{TiO}_2$ were used as photocatalyst, the changes of the peak intensity at 357 nm were also observed, but the changes were much slower (Fig. 9B and C). No obvious changes could be observed without any catalyst (Fig. 9D). After 20 min irradiation under visible light, the degradation rate of TCH were 76.5%, 59.6%, and 31.9% in the presence of $\text{AgBr}/\text{Ti}_3\text{C}_2@\text{TiO}_2$ -10%, AgBr , and $\text{Ti}_3\text{C}_2@\text{TiO}_2$, respectively. These results show that the photocatalytic performance of $\text{AgBr}/\text{Ti}_3\text{C}_2@\text{TiO}_2$ -10% is much better than that of pure AgBr and $\text{Ti}_3\text{C}_2@\text{TiO}_2$.

Similarly, $\text{AgBr}/\text{Ti}_3\text{C}_2@\text{TiO}_2$ composites with different $\text{Ti}_3\text{C}_2@\text{TiO}_2$ contents were used to degrade TCH. With increase of $\text{Ti}_3\text{C}_2@\text{TiO}_2$ content, the photodegradation efficiency of $\text{AgBr}/\text{Ti}_3\text{C}_2@\text{TiO}_2$ composites increased first and then decreased. The

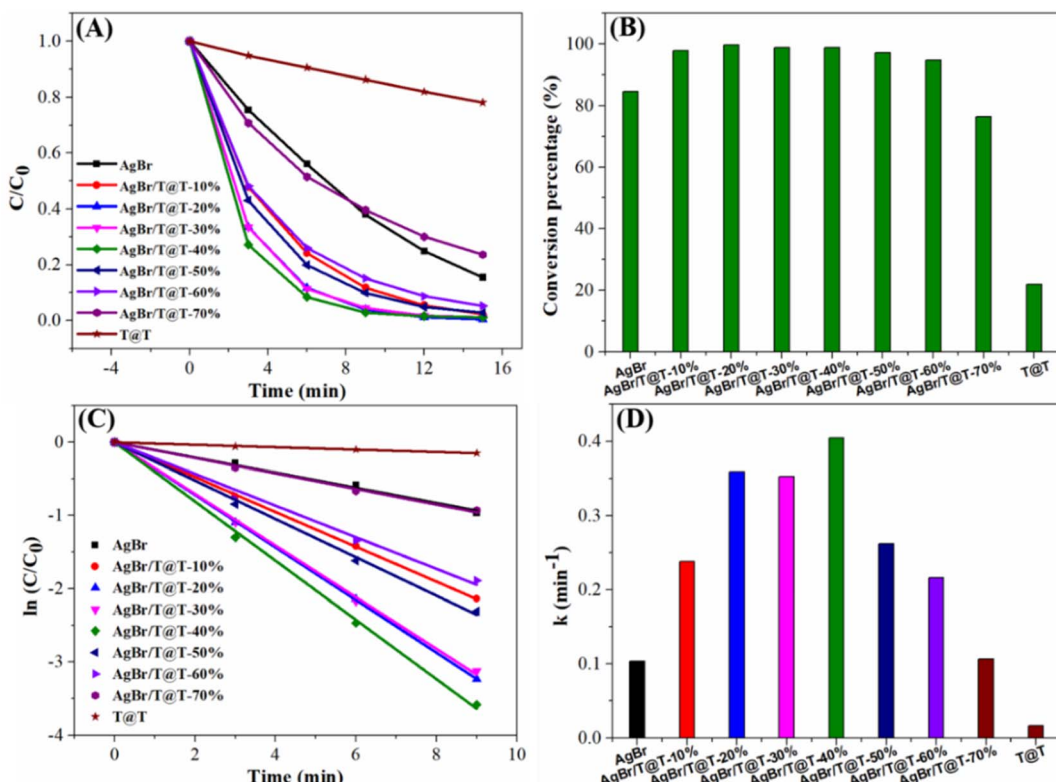


Fig. 8 AgBr , $\text{Ti}_3\text{C}_2@\text{TiO}_2$ (T@T for short) and $\text{AgBr}/\text{Ti}_3\text{C}_2@\text{TiO}_2$ - $x\%$ ($\text{AgBr}/\text{T@T-}x\%$ for short) photocatalytic oxidation of 1,4-DHP under visible light: (A) kinetic diagram, (B) degradation efficiency graph, (C) the linear kinetic fitting graph, (D) apparent rate constant.



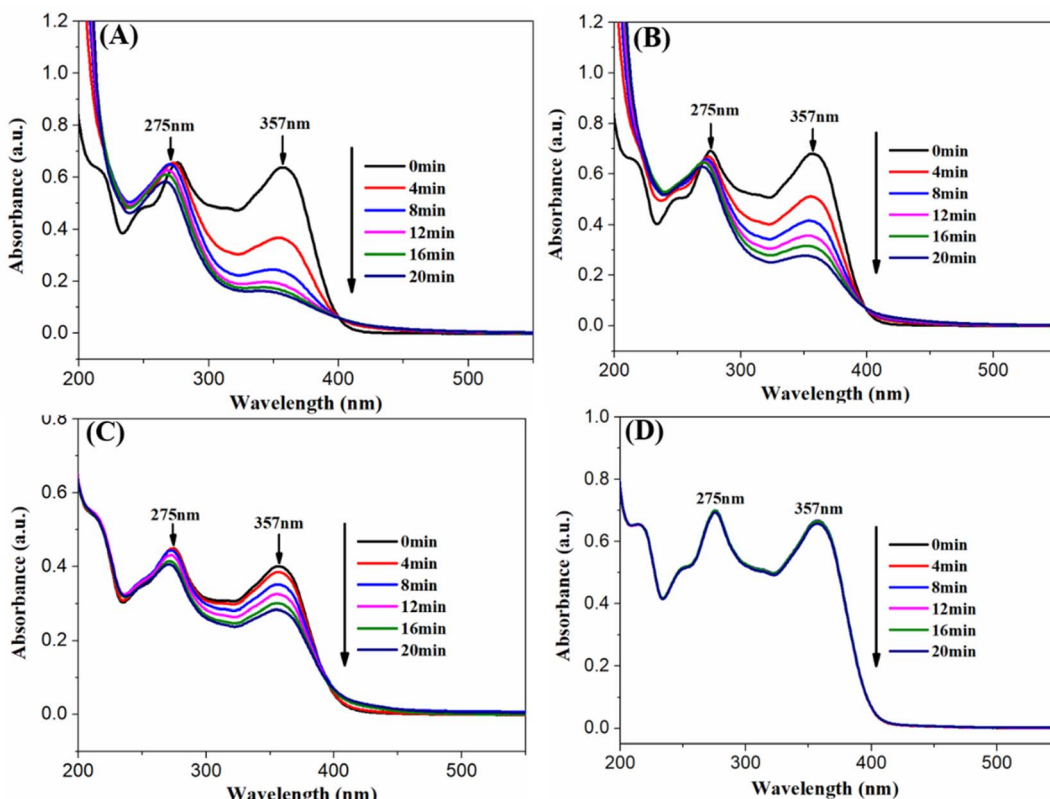


Fig. 9 Under the irradiation of visible light ($\lambda > 400$ nm), the ultraviolet-visible spectrum changes of TCH solution under different photocatalysts. (A) $\text{AgBr}/\text{Ti}_3\text{C}_2@\text{TiO}_2$ -10%, (B) AgBr , (C) $\text{Ti}_3\text{C}_2@\text{TiO}_2$ and (D) no catalyst.

photo-degradation results of TCH show that under visible light, the conversion rate of $\text{AgBr}/\text{Ti}_3\text{C}_2@\text{TiO}_2$ -10% to TCH reaches 76.5% within 20 min, showing the highest photocatalytic activity (Fig. 10A and B). The photodegradation rate constant of TCH (Fig. 10D) is obtained by plotting $\ln(C/C_0)$ vs. time in Fig. 10C. Among them, the rate constant of $\text{AgBr}/\text{Ti}_3\text{C}_2@\text{TiO}_2$ -10% is the highest (0.1027 min^{-1}), which is about 1.9 times and 5.9 times as high as that of pure AgBr (0.0540 min^{-1}) and $\text{Ti}_3\text{C}_2@\text{TiO}_2$ (0.0174 min^{-1}), respectively. The above data show that $\text{AgBr}/\text{Ti}_3\text{C}_2@\text{TiO}_2$ composite also has good photocatalytic performance for TCH degradation.

The UV-vis DRS spectra of the materials are shown in Fig. 11A. In comparison with pure AgBr , with an increase of $\text{Ti}_3\text{C}_2@\text{TiO}_2$ content, the light absorption ability of the composites gradually increases.^{45,56} The fast charge transfer properties of the prepared materials were analyzed by PL spectroscopy. As shown in Fig. 11B, compared with the pure AgBr , pure Ti_3C_2 and $\text{Ti}_3\text{C}_2@\text{TiO}_2$ samples, the emission peaks of the $\text{AgBr}/\text{Ti}_3\text{C}_2@\text{TiO}_2$ composite are of weaker intensity, indicating the beneficial effect of the heterojunction to promote the separation efficiency of photo-induced electron–hole pairs.^{35,57} Electrochemical impedance spectroscopy (EIS) tests are used to study the electrochemical performance. Fig. 11C shows the Nyquist diagram of EIS of AgBr , $\text{Ti}_3\text{C}_2@\text{TiO}_2$ and $\text{AgBr}/\text{Ti}_3\text{C}_2@\text{TiO}_2$ photocatalysts. In general, the arc radius in the Nyquist diagram describes the reaction rate at the electrode surface, the smaller the radius, the lower the corresponding

electron transfer resistance, the higher the charge transfer and separation efficiency.⁵⁸ The arc radii of $\text{AgBr}/\text{Ti}_3\text{C}_2@\text{TiO}_2$ composites are much smaller than that of pure AgBr and $\text{Ti}_3\text{C}_2@\text{TiO}_2$, which indicates that more efficient photogenerated charge carrier's separation, lower internal resistance and faster transfer of charge carriers can occur on the surface of $\text{AgBr}/\text{Ti}_3\text{C}_2@\text{TiO}_2$ composites. These results demonstrate that AgBr is successfully compounded with $\text{Ti}_3\text{C}_2@\text{TiO}_2$ and has good photogenerated charge carrier separation efficiency. Fig. 11D–F shows the Mott–Schottky curves of AgBr , $\text{Ti}_3\text{C}_2@\text{TiO}_2$ and $\text{AgBr}/\text{Ti}_3\text{C}_2@\text{TiO}_2$ -10% materials. As can be seen from the figure that AgBr is considered as an n-type semiconductor because of its positive slope (Fig. 11D). Although TiO_2 is also an n-type semiconductor,⁵⁹ its Mott–Schottky diagram slope of $\text{Ti}_3\text{C}_2@\text{TiO}_2$ composite material is negative after *in situ* growth on Ti_3C_2 by solvothermal method, and it has the potential of a p-type semiconductor^{2,23} (Fig. 11E). More importantly, the Mott–Schottky diagram of $\text{AgBr}/\text{Ti}_3\text{C}_2@\text{TiO}_2$ -10% composite shows an inverted “V-shape” as shown in Fig. 11F, which indicates that the p–n junction structure has been successfully formed.

Using $\text{AgBr}/\text{Ti}_3\text{C}_2@\text{TiO}_2$ composite catalyst, four repeated experiments were carried out to determine the photo-dehydrogenation of 1,4-DHP and the photodegradation of TCH separately to evaluate the stability of the prepared photocatalyst. After four cycles, the relative hydrogenation efficiency of 1,4-DHP was 86.2% (Fig. 12A and B), and the relative degradation efficiency of TCH was 93.8% (Fig. 12C and D). Part of the

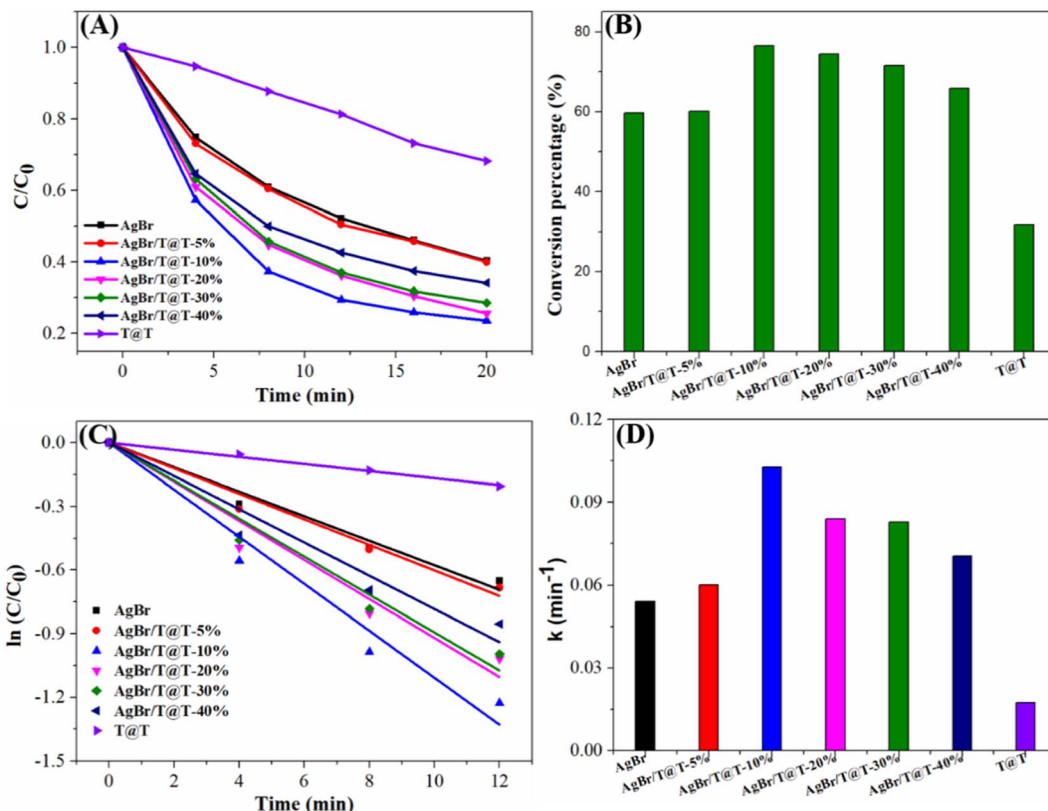


Fig. 10 AgBr, $\text{Ti}_3\text{C}_2@\text{TiO}_2$ (T@T for short) and $\text{AgBr}/\text{Ti}_3\text{C}_2@\text{TiO}_2-x\%$ ($\text{AgBr}/\text{T@T}-x\%$ for short) photocatalytic degradation of TCH under visible light: (A) kinetic diagram, (B) degradation efficiency graph, (C) the linear kinetic fitting graph, (D) apparent rate constant.

reason for the decrease in efficiency may be due to the loss of the catalyst during the cycle. Therefore, $\text{AgBr}/\text{Ti}_3\text{C}_2@\text{TiO}_2$ composite has good photocatalytic stability and potential practical application.

Active species capture experiment was conducted to explore the three main active species in photocatalytic reaction,⁶⁰ ammonium oxalate (AO), benzoquinone (BQ) and isopropanol (IPA) were used as scavengers for h^+ , $\cdot\text{O}_2^-$ and $\cdot\text{OH}$, respectively.⁵³ As shown in Fig. 13, the addition of IPA slightly decreased the degradation of TCH but has little effect on the dehydrogenation of 1,4-DHP, the addition of AO has a little effect on the degradation of TCH, but slightly decreased the dehydrogenation of 1,4-DHP. When BQ was added to the reaction system, the degradation of TCH was obviously inhibited (Fig. 13A), indicating the major role of $\cdot\text{O}_2^-$ in TCH degradation. The addition of BQ has significant influence on absorption spectrum of 1,4-DHP (data not shown), so BQ is not suitable for the detection of $\cdot\text{O}_2^-$ radicals in the reaction system of 1,4-DHP. It was generally thought that the dissolved oxygen (O_2) in the reaction solution accepted photo-excited electrons from the conduction band of a semiconductor to produce $\cdot\text{O}_2^-$ ($\text{O}_2 + \text{e}^- \rightarrow \cdot\text{O}_2^-$).⁶¹ Therefore, the removal of O_2 from the 1,4-DHP reaction system would affect the photodehydrogenation of 1,4-DHP, if $\cdot\text{O}_2^-$ was involved in the dehydrogenation process. With this in mind, we carried out the photodehydrogenation of 1,4-DHP under a nitrogen

atmosphere. The dissolved O_2 was removed from the reaction by nitrogen bubbling. The removal of O_2 apparently suppressed the dehydrogenation of 1,4-DHP (Fig. 13B). This results suggested that $\cdot\text{O}_2^-$ was also played important role in 1,4-DHP dehydrogenation, just as in TCH degradation.

EPR technique was employed to further detect the generation of $\cdot\text{O}_2^-$ in the $\text{AgBr}/\text{Ti}_3\text{C}_2@\text{TiO}_2$ composite involved photocatalytic system. DMPO was used as a radical trap. As shown in Fig. 13C, the DMPO- $\cdot\text{O}_2^-$ characteristic peak was observed under visible light irradiation,⁶² but not observed in dark condition. The production of $\cdot\text{OH}$ by $\text{AgBr}/\text{Ti}_3\text{C}_2@\text{TiO}_2$ composite during the photocatalysis process was probed by fluorescence technique.⁶³ The fluorescence absorption peak around 425 nm obviously increased with visible-light irradiation time (Fig. 13D), indicating the formation of hydroxyl terephthalic acid (TA-OH), confirmed the generation of $\cdot\text{OH}$ on the surface of $\text{AgBr}/\text{Ti}_3\text{C}_2@\text{TiO}_2$ composites.⁵³

According to the results of active species capture experiment, EPR trapping experiment and terephthalic acid-based fluorescence experiment, a possible photocatalytic reaction mechanism was proposed (Fig. 14).

Under the excitation of visible light, AgBr with narrow band gap (2.6 eV) absorbs photons and produces photo-generated electron-hole pairs (eqn (1)). According to theoretical analysis, the conduction band (CB) potential of AgBr is more negative than the CB potential of TiO_2 and the Fermi



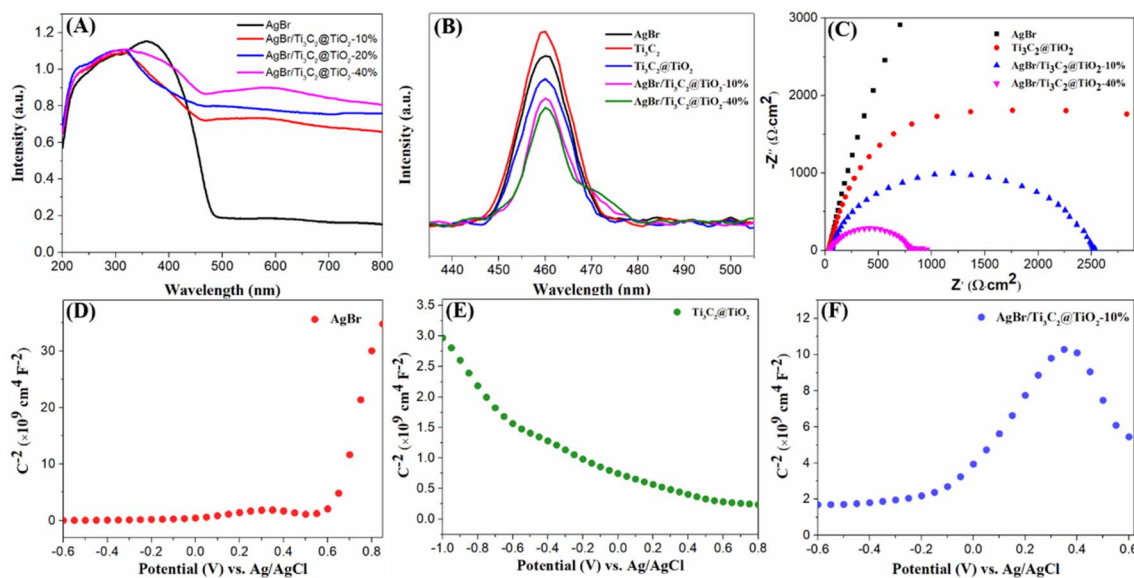


Fig. 11 UV-vis DRS of the as-prepared samples (A), PL spectra (B), EIS Nyquist plots of samples (C), Mott–Schottky plots of AgBr (D), $\text{Ti}_3\text{C}_2\text{@TiO}_2$ (E) and $\text{AgBr}/\text{Ti}_3\text{C}_2\text{@TiO}_2\text{-}10\%$ (F).

level of Ag^0 nanoparticles.^{64–66} Therefore, the electrons on the CB of AgBr can rapidly transfer to the CB of TiO_2 (eqn (2)) or be captured by Ag^0 nanoparticles through Schottky barrier (eqn (3)).⁶⁷ The electrons on the CB of TiO_2 can further

transfer to Ti_3C_2 (eqn (4)), since the CB potentials of TiO_2 is more negative than the Fermi level of the Ti_3C_2 .^{30,68,69} Thus, the photoinduced charge carriers on AgBr is efficiently separated, and the photocatalytic activity of AgBr is improved by

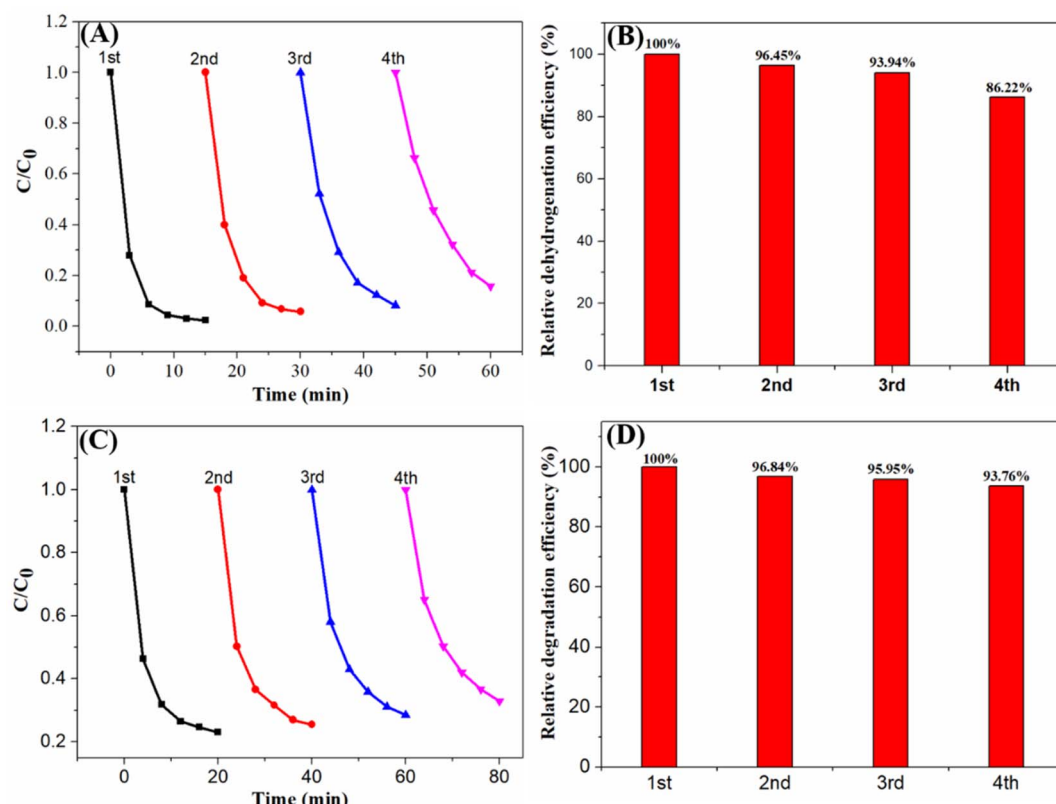


Fig. 12 Cyclic kinetics curve and relative dehydrogenation efficiency of 1,4-DHP by $\text{AgBr}/\text{Ti}_3\text{C}_2\text{@TiO}_2\text{-}40\%$ (A and B); cyclic kinetics curve and relative degradation efficiency of TCH by $\text{AgBr}/\text{Ti}_3\text{C}_2\text{@TiO}_2\text{-}10\%$ (C and D).

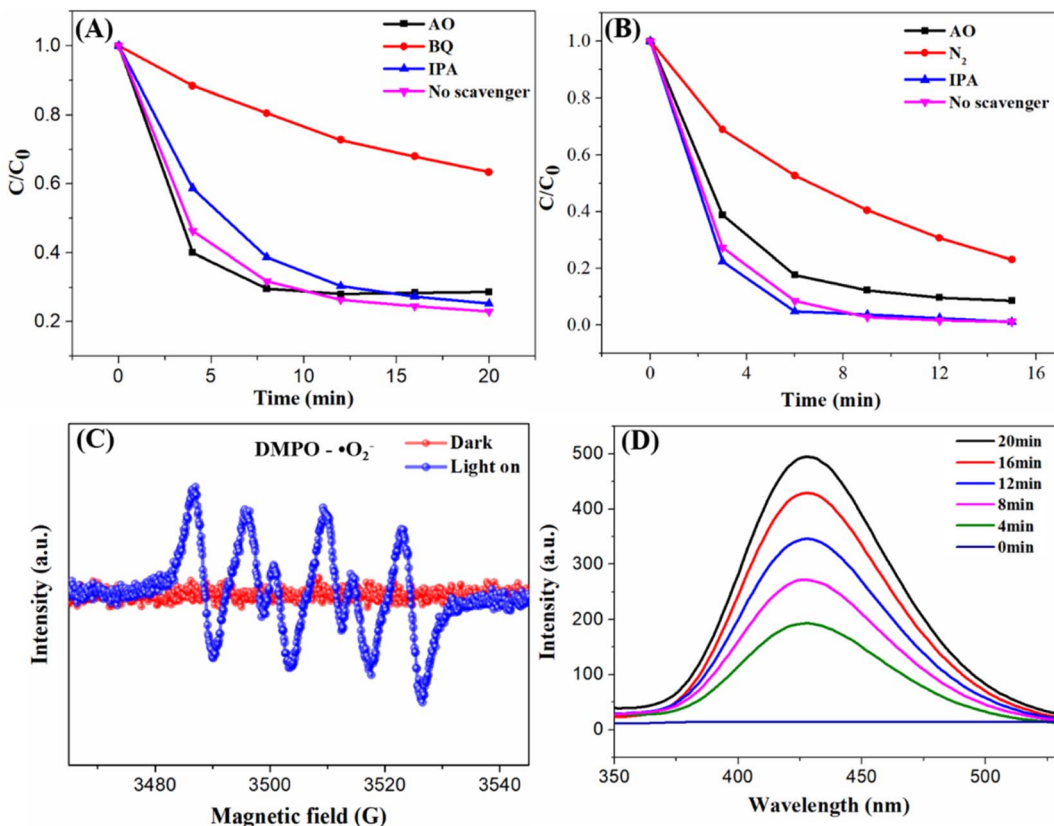
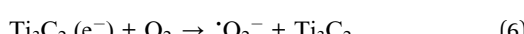
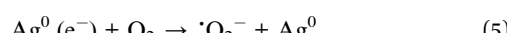
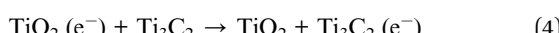
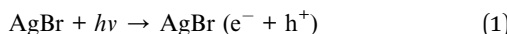


Fig. 13 The effect of certain selected scavengers on the photooxidation of TCH (A) and 1,4-DHP (B) under visible light ($\lambda > 400$ nm) irradiation, EPR signals of AgBr/Ti₃C₂@TiO₂ under dark and visible light irradiation (C) and fluorescence spectra of 0.5 mM alkaline terephthalic acid (TA) solution in the presence of AgBr/Ti₃C₂@TiO₂ composite under visible light irradiation (D).

compositing with Ti₃C₂@TiO₂. The electrons transferred to Ag⁰ and Ti₃C₂ are subsequently captured by O₂ to produce 'O₂⁻' (eqn (5) and (6)). At the same time, the h⁺ left on the valence band (VB) of AgBr can convert H₂O and OH⁻ (H₂O/OH⁻) to 'OH (eqn (7)). The produced 'O₂⁻', 'OH and h⁺ may all be utilized as oxidizer for 1,4-DHP dehydrogenation and TCH degradation (eqn (8)).



It is worth pointing out that the main active species are 'O₂⁻ and h⁺ for 1,4-DHP dehydrogenation, while 'O₂⁻ and 'OH for TCH degradation. In other words, the photogenerated

h⁺ in the VB of AgBr can react with H₂O and OH⁻ to produce 'OH, then the generated 'OH is consumed by the oxidation of TCH in the TCH-catalyst system. But for the 1,4-DHP-catalyst system, the generated 'OH cannot be consumed by 1,4-DHP, which will influence the separation of photogenerated electron-hole pairs. The transfer of electrons in the CB of AgBr to separate it from the photogenerated holes in the VB of AgBr is more urgent in the 1,4-DHP-catalysts system. Therefore, the introduction of Ti₃C₂@TiO₂ into AgBr is more pronounced to enhance the catalytic activity of AgBr for 1,4-DHP oxidation. This maybe also one of the reasons that the optimal proportion of Ti₃C₂@TiO₂ is different for 1,4-DHP and TCH.

To sum up, under visible light irradiation, The enhanced photocatalytic performance of AgBr/Ti₃C₂@TiO₂ composite should be attributed to the following aspects: (1) the formation of a p-n heterojunction between AgBr and TiO₂ and the introduction of Ti₃C₂ as an electron transport medium and acceptor can rapidly transfer electrons, thus enhancing the separation rate of photo-generated electron-hole pairs; (2) as the size of AgBr particles in the composite decreases, the specific surface area of the composite increases, and the contact area between the interfaces of AgBr, TiO₂ and Ti₃C₂ increases, which also promotes the transfer of photogenerated carriers. (3) Ti₃C₂ and AgBr has good absorption capacity for visible light, which can increase the utilization of visible light by composite materials.



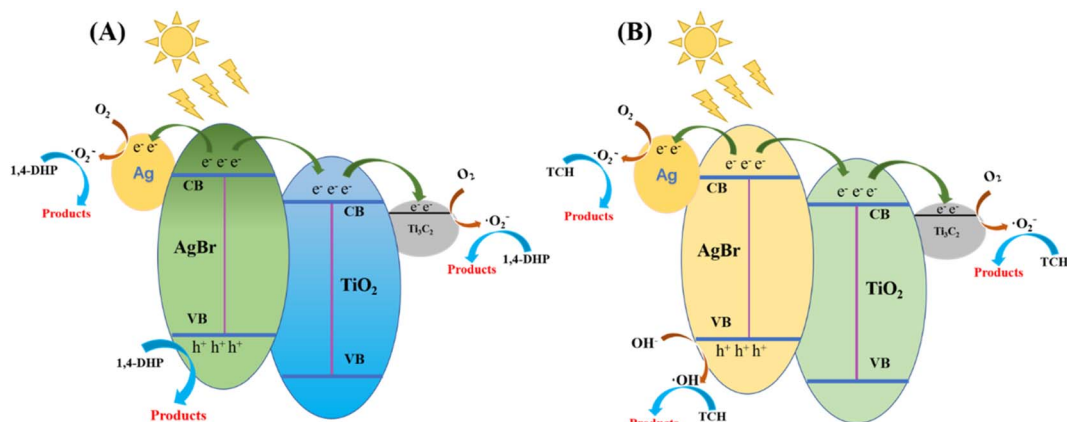


Fig. 14 Hypothetical mechanism diagram of dehydrogenation of 1,4-DHP (A) and photodegradation of TCH (B) by AgBr/Ti₃C₂@TiO₂ composites under visible light ($\lambda > 400$ nm).

4. Conclusions

In conclusion, AgBr/Ti₃C₂@TiO₂ composite photocatalyst was prepared by solvothermal and precipitation method and the photocatalytic performance of the composite was evaluated by the photodehydrogenation of 1,4-DHP and photodegradation of TCH under visible light irradiation. The AgBr/Ti₃C₂@TiO₂ composite photocatalyst showed improved photocatalytic performance compared with AgBr and Ti₃C₂@TiO₂. The photocatalytic performance of the AgBr/Ti₃C₂@TiO₂ composite with optimized composition is 3.9 and 24.5 times higher than that of pure AgBr and Ti₃C₂@TiO₂, respectively, for photodehydrogenation of 1,4-DHP and 1.9 and 5.9 times higher than that of pure AgBr and Ti₃C₂@TiO₂ for photodegradation of TCH. The improvement of photocatalytic performance of AgBr/Ti₃C₂@TiO₂ composite is due to the formation of p-n heterojunction structure between AgBr and Ti₃C₂@TiO₂, and the using of Ti₃C₂ as cocatalyst, which reduced the internal resistance, accelerated charge transfer and improved the separation efficiency of photo-generated carriers. In addition, AgBr/Ti₃C₂@TiO₂ composite photocatalyst also showed good stability in photochemical reaction, indicating that the AgBr/Ti₃C₂@TiO₂ composite has potential application in photooxidation reaction, wastewater treatment and environmental remediation.

Conflicts of interest

There are no conflicts of interest to declare.

Acknowledgements

This work was supported by the Opening Project of Key Laboratory of Green Chemistry of Sichuan Institutes of Higher Education (LZJ2002) and the Open Project of Chemical Synthesis and Pollution Control Key Laboratory of Sichuan Province (CSPC2016-3-2).

References

- 1 X. Shi, B. Ren, X. Jin, X. C. Wang and P. Jin, Metabolic hazards of pharmaceuticals and personal care products (PPCPs) in sewers, *J. Hazard. Mater.*, 2022, **432**, 128539.
- 2 S. Li, Y. Wang, J. Wang, J. Liang, Y. Li and P. Li, Modifying g-C₃N₄ with oxidized Ti₃C₂ MXene for boosting photocatalytic U(VI) reduction performance, *J. Mol. Liq.*, 2022, **346**, 117937.
- 3 P. Zhang, J. Xu, X.-J. Wang, B. He, S.-Q. Gao and Y.-W. Lin, The Third Generation of Artificial Dye-Decolorizing Peroxidase Rationally Designed in Myoglobin, *ACS Catal.*, 2019, **9**, 7888–7893.
- 4 D. Ren, R. Shen, Z. Jiang, X. Lu and X. Li, Highly efficient visible-light photocatalytic H₂ evolution over 2D-2D CdS/Cu₇S₄ layered heterojunctions, *Chin. J. Catal.*, 2020, **41**, 31–40.
- 5 C. Bie, H. Yu, B. Cheng, W. Ho, J. Fan and J. Yu, Design, Fabrication, and Mechanism of Nitrogen-Doped Graphene-Based Photocatalyst, *Adv. Mater.*, 2021, **33**, 2003521.
- 6 X. Bao, D. Lu, Z. Wang, H. Yin, B. Zhu, B. Chen, M. Shi, Y. Zhang, Q. Xu, Y. Qin, X. C. Shen and K. Wu, Significantly enhanced photothermal catalytic CO₂ reduction over TiO₂/g-C₃N₄ composite with full spectrum solar light, *J. Colloid Interface Sci.*, 2023, **638**, 63–75.
- 7 M. Tian, J. Wang, R. Sun, D. Lu, N. Li, T. Liu, M. Yao, G. Zhang and L. Li, Facile synthesis of rod-like TiO₂-based composite loaded with g-C₃N₄ for efficient removal of high-chroma organic pollutants based on adsorption-photocatalysis mechanism, *Inorg. Chem. Commun.*, 2022, **141**, 109517.
- 8 Y. Elviera, D. O. B. Yulizar, R. Apriandanan and S. Marcony, Fabrication of novel SnWO₄/ZnO using Muntingia calabura L. leaf extract with enhanced photocatalytic methylene blue degradation under visible light irradiation, *Ceram. Int.*, 2022, **48**, 3564–3577.
- 9 P. Hemmatpour and A. Nezamzadeh-Ejhieh, A Z-scheme CdS/BiVO₄ photocatalysis towards Eriochrome black T: An experimental design and mechanism study, *Chemosphere*, 2022, **307**, 135925.



10 H. Lu, Y. Liu, S. Zhang, J. Wan, X. Wang, L. Deng, J. Kan and G. Wu, Clustered tubular S-scheme ZnO/CdS heterojunctions for enhanced photocatalytic hydrogen production, *Mater. Sci. Eng., B*, 2023, **289**, 116282.

11 T. Ren, Y. Dang, Y. Xiao, Q. Hu, D. Deng, J. Chen and P. He, Depositing Ag nanoparticles on g-C₃N₄ by facile silver mirror reaction for enhanced photocatalytic hydrogen production, *Inorg. Chem. Commun.*, 2021, **123**, 108367.

12 F. Dong, Z. Wang, Y. Li, W. K. Ho and S. C. Lee, Immobilization of polymeric g-C₃N₄ on structured ceramic foam for efficient visible light photocatalytic air purification with real indoor illumination, *Environ. Sci. Technol.*, 2014, **48**, 10345–10353.

13 Z. Miao, G. Wang, X. Zhang and X. Dong, Oxygen vacancies modified $\text{TiO}_2/\text{Ti}_3\text{C}_2$ derived from MXenes for enhanced photocatalytic degradation of organic pollutants: The crucial role of oxygen vacancy to Schottky junction, *Appl. Surf. Sci.*, 2020, **528**, 146929.

14 Y. Yan, X. Zhou, P. Yu, Z. Li and T. Zheng, Characteristics, mechanisms and bacteria behavior of photocatalysis with a solid Z-scheme Ag/AgBr/g-C₃N₄ nanosheet in water disinfection, *Appl. Catal., A*, 2020, **590**, 117282.

15 A. Ren, C. Liu, Y. Hong, W. Shi, S. Lin and P. Li, Enhanced visible-light-driven photocatalytic activity for antibiotic degradation using magnetic $\text{NiFe}_2\text{O}_4/\text{Bi}_2\text{O}_3$ heterostructures, *Chem. Eng. J.*, 2014, **258**, 301–308.

16 Y. Shi, Z. Yan, Y. Xu, T. Tian, J. Zhang, J. Pang, X. Peng, Q. Zhang, M. Shao, W. Tan, H. Li and Q. Xiong, Visible-light-driven AgBr– TiO_2 –Palygorskite photocatalyst with excellent photocatalytic activity for tetracycline hydrochloride, *J. Cleaner Prod.*, 2020, **277**, 124021.

17 P. Laokul, N. Kanjana, R. Ratchatanee, S. Ruangjan, N. Kotsarn, A. Chingsungnoen and P. Poolcharuansin, Preparation of AgBr decorated ZnO/ZnS nanocomposite for photocatalytic and antibacterial applications, *Mater. Chem. Phys.*, 2023, **295**, 127112.

18 X. Xue, X. Chen, Z. Zhang, G. Fan and T. Ma, Improved ionic organic pollutant degradation under visible light by Ag SPR-promoted phosphorus-doped g-C₃N₄/AgBr/Bi₂WO₆ with excellent charge transfer capacity and high surface area, *J. Alloys Compd.*, 2023, **930**, 167457.

19 W. Wang, L. Jing, Y. Qu, Y. Luan, H. Fu and Y. Xiao, Facile fabrication of efficient AgBr– TiO_2 nanoheterostructured photocatalyst for degrading pollutants and its photogenerated charge transfer mechanism, *J. Hazard. Mater.*, 2012, **243**, 169–178.

20 K. Dai, J. Lv, L. Lu, Q. Liu, G. Zhu and D. Li, Synthesis of micro-nano heterostructure AgBr/ZnO composite for advanced visible light photocatalysis, *Mater. Lett.*, 2014, **130**, 5–8.

21 P. Singh, Sonu, P. Raizada, A. Sudhaik, P. Shandilya, P. Thakur, S. Agarwal and V. K. Gupta, Enhanced photocatalytic activity and stability of AgBr/BiOBr/graphene heterojunction for phenol degradation under visible light, *J. Saudi Chem. Soc.*, 2019, **23**, 586–599.

22 M. Abou Asi, C. He, M. Su, D. Xia, L. Lin, H. Deng, Y. Xiong, R. Qiu and X.-Z. Li, Photocatalytic reduction of CO₂ to hydrocarbons using AgBr/TiO₂ nanocomposites under visible light, *Catal. Today*, 2011, **175**, 256–263.

23 Y. Cui, Z. Zhang, B. Li, R. Guo, X. Zhang, X. Cheng, M. Xie and Q. Cheng, Ultrasound assisted fabrication of AgBr/TiO₂ nano-tube arrays photoelectrode and its enhanced visible photocatalytic performance and mechanism for detoxification of 4-chlorophenol, *Sep. Purif. Technol.*, 2018, **197**, 189–196.

24 M. Naguib, M. Kurtoglu, V. Presser, J. Lu, J. Niu, M. Heon, L. Hultman, Y. Gogotsi and M. W. Barsoum, Two-dimensional nanocrystals produced by exfoliation of Ti_3AlC_2 , *Adv. Mater.*, 2011, **23**, 4248–4253.

25 R. Zhao, M. Wang, D. Zhao, H. Li, C. Wang and L. Yin, Molecular-Level Heterostructures Assembled from Titanium Carbide MXene and Ni–Co–Al Layered Double-Hydroxide Nanosheets for All-Solid-State Flexible Asymmetric High-Energy Supercapacitors, *ACS Energy Lett.*, 2017, **3**, 132–140.

26 Y. Yang, D. Zhang and Q. Xiang, Plasma-modified $\text{Ti}_3\text{C}_2\text{T}_{x}/\text{CdS}$ hybrids with oxygen-containing groups for high-efficiency photocatalytic hydrogen production, *Nanoscale*, 2019, **11**, 18797–18805.

27 M. Wu, M. He, Q. Hu, Q. Wu, G. Sun, L. Xie, Z. Zhang, Z. Zhu and A. Zhou, Ti_3C_2 MXene-Based Sensors with High Selectivity for NH₃ Detection at Room Temperature, *ACS Sens.*, 2019, **4**, 2763–2770.

28 J. Guo, Q. Peng, H. Fu, G. Zou and Q. Zhang, Heavy-Metal Adsorption Behavior of Two-Dimensional Alkalization-Intercalated MXene by First-Principles Calculations, *J. Phys. Chem. C*, 2015, **119**, 20923–20930.

29 C. Cai, R. Wang, S. Liu, X. Yan, L. Zhang, M. Wang, Q. Tong and T. Jiao, Synthesis of self-assembled phytic acid-MXene nanocomposites via a facile hydrothermal approach with elevated dye adsorption capacities, *Colloids Surf., A*, 2020, **589**, 124468.

30 J. Low, L. Zhang, T. Tong, B. Shen and J. Yu, $\text{TiO}_2/\text{MXene}$ Ti_3C_2 composite with excellent photocatalytic CO₂ reduction activity, *J. Catal.*, 2018, **361**, 255–266.

31 Z. Liu, Y. Zhou, L. Yang and R. Yang, Green preparation of *in situ* oxidized $\text{TiO}_2/\text{Ti}_3\text{C}_2$ heterostructure for photocatalytic hydrogen production, *Adv. Powder Technol.*, 2021, **32**, 4857–4861.

32 B. Tan, Y. Fang, Q. Chen, X. Ao and Y. Cao, Construction of $\text{Bi}_2\text{O}_2\text{CO}_3/\text{Ti}_3\text{C}_2$ heterojunctions for enhancing the visible-light photocatalytic activity of tetracycline degradation, *J. Colloid Interface Sci.*, 2021, **601**, 581–593.

33 B. Sun, F. Tao, Z. Huang, W. Yan, Y. Zhang, X. Dong, Y. Wu and G. Zhou, Ti_3C_2 MXene-bridged Ag/Ag₃PO₄ hybrids toward enhanced visible-light-driven photocatalytic activity, *Appl. Surf. Sci.*, 2021, **535**, 147354.

34 Y. Cao, L. Yue, Z. Li, Y. Han, J. Lian, H. Qin and S. He, Construction of Sn-Bi-MOF/Ti₃C₂ Schottky junction for photocatalysis of tetracycline: Performance and degradation mechanism, *Appl. Surf. Sci.*, 2023, **609**, 155191.

35 H. Wang, R. Zhao, J. Qin, H. Hu, X. Fan, X. Cao and D. Wang, MIL-100(Fe)/Ti₃C₂ MXene as a Schottky Catalyst with



Enhanced Photocatalytic Oxidation for Nitrogen Fixation Activities, *ACS Appl. Mater. Interfaces*, 2019, **11**, 44249–44262.

36 Y. Li, X. Deng, J. Tian, Z. Liang and H. Cui, Ti₃C₂ MXene-derived Ti₃C₂/TiO₂ nanoflowers for noble-metal-free photocatalytic overall water splitting, *Appl. Mater. Today*, 2018, **13**, 217–227.

37 J. Shu, Z. Wang, G. Xia, Y. Zheng, L. Yang and W. Zhang, One-pot synthesis of AgCl@Ag hybrid photocatalyst with high photocatalytic activity and photostability under visible light and sunlight irradiation, *Chem. Eng. J.*, 2014, **252**, 374–381.

38 G. Zou, Z. Zhang, J. Guo, B. Liu, Q. Zhang, C. Fernandez and Q. Peng, Synthesis of MXene/Ag Composites for Extraordinary Long Cycle Lifetime Lithium Storage at High Rates, *ACS Appl. Mater. Interfaces*, 2016, **8**, 22280–22286.

39 C. Xu, D. Li, H. Liu, D. Wang, X. Liu, S. Lin, Y. Yang, D. Fan and H. Pan, Construction of 1D/0D CdS nanorods/Ti₃C₂ QDs Schottky heterojunctions for efficient photocatalysis, *J. Environ. Chem. Eng.*, 2023, **11**, 109191.

40 Y. Wang, X. Wang, Y. Ji, R. Bian, J. Li, X. Zhang, J. Tian, Q. Yang and F. Shi, Ti₃C₂ MXene coupled with CdS nanoflowers as 2D/3D heterostructures for enhanced photocatalytic hydrogen production activity, *Int. J. Hydrogen Energy*, 2022, **47**, 22045–22053.

41 H. Liu, C. Yang, X. Jin, J. Zhong and J. Li, One-pot hydrothermal synthesis of MXene Ti₃C₂/TiO₂/BiOCl ternary heterojunctions with improved separation of photoactivated carries and photocatalytic behavior toward elimination of contaminants, *Colloids Surf., A*, 2020, **603**, 125239.

42 X. Liu, D. Zhang, B. Guo, Y. Qu, G. Tian, H. Yue and S. Feng, Recyclable and visible light sensitive Ag–AgBr/TiO₂: Surface adsorption and photodegradation of MO, *Appl. Surf. Sci.*, 2015, **353**, 913–923.

43 K. Huang, C. Lv, C. Li, H. Bai and X. Meng, Ti₃C₂ MXene supporting platinum nanoparticles as rapid electrons transfer channel and active sites for boosted photocatalytic water splitting over g-C₃N₄, *J. Colloid Interface Sci.*, 2023, **636**, 21–32.

44 W. Li, H. Chen, Y. Liu, T. Cai, W. Dong and X. Xia, A novel Ti₃C₂ MXene/PDI supramolecules composite with enhanced photocatalytic activities for degradation of tetracycline hydrochloride under visible-light, *J. Environ. Chem. Eng.*, 2022, **10**, 107978.

45 B. Saini, K. Harikrishna, D. Laishram, R. Krishnapriya, R. Singhal and R. K. Sharma, Role of ZnO in ZnO Nanoflake/Ti₃C₂ MXene Composites in Photocatalytic and Electrocatalytic Hydrogen Evolution, *ACS Appl. Nano Mater.*, 2022, **5**, 9319–9333.

46 D. Chen, M. Liu, Q. Chen, L. Ge, B. Fan, H. Wang, H. Lu, D. Yang, R. Zhang, Q. Yan, G. Shao, J. Sun and L. Gao, Large-scale synthesis and enhanced visible-light-driven photocatalytic performance of hierarchical Ag/AgCl nanocrystals derived from freeze-dried PVP-Ag⁺ hybrid precursors with porosity, *Appl. Catal., B*, 2014, **144**, 394–407.

47 Z. Zhang, J. Yu, L. Ma, Y. Sun, P. Wang, T. Wang and S. Peng, Preparation of the plasmonic Ag/AgBr/ZnO film substrate for reusable SERS detection: Implication to the Z-scheme photocatalytic mechanism, *Spectrochim. Acta, Part A*, 2020, **224**, 117381.

48 X. Peng, J. Tian, S. Zhang, W. Xiao, X. Tian, Y. Wang, J. Xue and D. Lei, Z-scheme transfer pathway assisted photoelectrocatalyst Zn₂SnO₄/rGO/Ag/AgBr for organic pollutants treatment, *Colloids Surf., A*, 2023, **657**, 130552.

49 L. Xiu, Z. Wang, M. Yu, X. Wu and J. Qiu, Aggregation-resistant 3D MXene-based architecture as efficient bifunctional electrocatalyst for overall water splitting, *ACS Nano*, 2018, **12**, 8017–8028.

50 N. Liu, N. Lu, H. Yu, S. Chen and X. Quan, Efficient day-night photocatalysis performance of 2D/2D Ti₃C₂/porous g-C₃N₄ nanolayers composite and its application in the degradation of organic pollutants, *Chemosphere*, 2020, **246**, 125760.

51 Z. Mao, W. Hao, W. Wang, F. Ma, C. Ma and S. Chen, BiO₁@CeO₂@Ti₃C₂ MXene composite S-scheme photocatalyst with excellent bacteriostatic properties, *J. Colloid Interface Sci.*, 2022, **633**, 836–850.

52 S. Shen, T. Ke, D. Fang and D. Lin, N and S co-doping of TiO₂@C derived from *in situ* oxidation of Ti₃C₂ MXene for efficient persulfate activation and sulfamethoxazole degradation under visible light, *Sep. Purif. Technol.*, 2022, **297**, 121460.

53 X. Tian, H. Wu, X. Hu, Z. Wang, C. Ren, Z. Cheng, L. Dou and Y.-W. Lin, Enhanced photocatalytic performance of ZnO/AgCl composites prepared by high-energy mechanical ball milling, *New J. Chem.*, 2022, **46**, 9155–9171.

54 Y. Cheng, L. He, G. Xia, C. Ren and Z. Wang, Nanostructured g-C₃N₄/AgI composites assembled by AgI nanoparticles-decorated g-C₃N₄ nanosheets for effective and mild photooxidation reaction, *New J. Chem.*, 2019, **43**, 14841–14852.

55 J. Zhang, X. An, N. Lin, W. Wu, L. Wang, Z. Li, R. Wang, Y. Wang, J. Liu and M. Wu, Engineering monomer structure of carbon nitride for the effective and mild photooxidation reaction, *Carbon*, 2016, **100**, 450–455.

56 H. Li, B. Sun, T. Gao, H. Li, Y. Ren and G. Zhou, Ti₃C₂ MXene co-catalyst assembled with mesoporous TiO₂ for boosting photocatalytic activity of methyl orange degradation and hydrogen production, *Chin. J. Catal.*, 2022, **43**, 461–471.

57 X. Zhang, H. Zhang, J. Yu, Z. Wu and Q. Zhou, Preparation of flower-like Co₃O₄ QDs/Bi₂WO₆ p–n heterojunction photocatalyst and its degradation mechanism of efficient visible-light-driven photocatalytic tetracycline antibiotics, *Appl. Surf. Sci.*, 2022, **585**, 152547.

58 S. Li, L. Shao, Z. Yang, S. Cheng, C. Yang, Y. Liu and X. Xia, Constructing Ti₃C₂ MXene/ZnIn₂S₄ heterostructure as a Schottky catalyst for photocatalytic environmental remediation, *Green Energy Environ.*, 2022, **7**, 246–256.

59 W. Gan, J. Zhang, H. Niu, L. Bao, H. Hao, Y. Yan, K. Wu and X. Fu, Fabrication of Ag/AgBr/TiO₂ composites with enhanced solar-light photocatalytic properties, *Colloids Surf., A*, 2019, **583**, 123968.

60 B. Zhou, H. Hong, H. Zhang, S. Yu and H. Tian, Heterostructured Ag/g-C₃N₄/TiO₂ with enhanced visible



light photocatalytic performances, *J. Chem. Technol. Biotechnol.*, 2019, **94**, 3806–3814.

61 Y. Ren, D. Guo, Z. Zhao, P. Chen, F. Li, J. Yao, H. Jiang and Y. Liu, Singlet oxygen mediated photocatalytic Antimonite decontamination in water using nanoconfined TiO_2 , *Chem. Eng. J.*, 2022, **435**, 134832.

62 H. Sun, C. Zou and W. Tang, Designing double Z-scheme heterojunction of $\text{g-C}_3\text{N}_4/\text{Bi}_2\text{MoO}_6/\text{Bi}_2\text{WO}_6$ for efficient visible-light photocatalysis of organic pollutants, *Colloids Surf. A*, 2022, **654**, 130105.

63 H. Huang, N. Huang, Z. Wang, G. Xia, M. Chen, L. He, Z. Tong and C. Ren, Room-temperature synthesis of carnation-like $\text{ZnO}@\text{AgI}$ hierarchical nanostructures assembled by AgI nanoparticles-decorated ZnO nanosheets with enhanced visible light photocatalytic activity, *J. Colloid Interface Sci.*, 2017, **502**, 77–88.

64 Y. Wang, H. Yang, H. Yun, J. Gao, Y. Liu, M. Zhang, G. He and Z. Sun, Crystallization time-induced microstructural evolution and photoelectrochemical properties of ternary $\text{Ag}@\text{AgBr}/\text{TiO}_2$ nanorod arrays, *J. Alloys Compd.*, 2022, **904**, 163370.

65 B. Chen, X. Chen, R. Li, W. Fan, F. Wang, B. Mao and W. Shi, Flame Reduced TiO_2 Nanorod Arrays with Ag Nanoparticle Decoration for Efficient Solar Water Splitting, *Ind. Eng. Chem. Res.*, 2019, **58**, 4818–4827.

66 K. Dai, D. Li, L. Lu, Q. Liu, C. Liang, J. Lv and G. Zhu, Plasmonic $\text{TiO}_2/\text{AgBr}/\text{Ag}$ ternary composite nanosphere with heterojunction structure for advanced visible light photocatalyst, *Appl. Surf. Sci.*, 2014, **314**, 864–871.

67 Y. Wan, C. Liang, Y. Xia, W. Huang and Z. Li, Fabrication of graphene oxide enwrapped Z-scheme $\text{Ag}_2\text{SO}_3/\text{AgBr}$ nanoparticles with enhanced visible-light photocatalysis, *Appl. Surf. Sci.*, 2017, **396**, 48–57.

68 V. Q. Hieu, T. K. Phung, T. Q. Nguyen, A. Khan, V. D. Doan, V. A. Tran and V. T. Le, Photocatalytic degradation of methyl orange dye by $\text{Ti}_3\text{C}_2\text{-TiO}_2$ heterojunction under solar light, *Chemosphere*, 2021, **276**, 130154.

69 M. A. Hossen, H. M. Solayman, K. H. Leong, L. C. Sim, N. Yaacof, A. Abd Aziz, L. Wu and M. U. Monir, Recent progress in TiO_2 -Based photocatalysts for conversion of CO_2 to hydrocarbon fuels: A systematic review, *Results Eng.*, 2022, **16**, 100795.

